



# Mechanical and microstructural characterization of powder metallurgy CoCrNi medium entropy alloy



Igor Moravcik<sup>a,\*</sup>, Jan Cizek<sup>b</sup>, Zuzana Kovacova<sup>c</sup>, Jitka Nejezchlebova<sup>d</sup>, Michael Kitzmantel<sup>c</sup>, Erich Neubauer<sup>c</sup>, Ivo Kubena<sup>e</sup>, Vit Hornik<sup>e</sup>, Ivo Dlouhy<sup>a</sup>

<sup>a</sup> NETME Centre, Institute of Materials Science and Engineering, Brno University of Technology, Technicka 2896/2, Brno, Czech Republic

<sup>b</sup> Institute of Plasma Physics, Czech Academy of Sciences, Za Slovankou 1782/3, 182 00 Prague 8, Czech Republic

<sup>c</sup> RHP-Technology GmbH, Forschungs, und Technologiezentrum, 2444 Seibersdorf, Austria

<sup>d</sup> Faculty of Nuclear Sciences and Physical Engineering, Czech Technical University in Prague, Trojanova 13, 18200 Prague, Czech Republic

<sup>e</sup> Institute of Physics of Materials CAS, Zizkova 22, 61662 Brno, Czech Republic

## ARTICLE INFO

### Keywords:

Tensile test  
Mechanical alloying  
Plasticity  
Mechanical characterization  
Powder metallurgy

## ABSTRACT

The present study is focused on synthesis and mechanical properties characterization of equiatomic CoCrNi medium entropy alloy (MEA). Powder metallurgy processes of mechanical alloying (MA) with subsequent spark plasma sintering (SPS) for bulk alloy densification have been utilized. As opposed to the single-phase alloys of identical composition fabricated via casting routes, the alloy after SPS compaction consisted of a major FCC solid solution phase (94.4%), minor fraction of secondary BCC phase (5.6%, precipitated at the FCC grains boundaries), and negligible amount of oxide inclusions. The alloy exhibited high ultimate tensile strength of 1024 MPa and a elongation to fracture of 26%. Elastic modulus of the alloy reached 222 GPa and the thermal expansion coefficient (CTE) was measured as  $17.4 \times 10^{-6} \text{ K}^{-1}$ . The plastic deformation in the alloy is carried out by a combination of dislocation glide and mechanical nano-twinning at room temperature.

## 1. Introduction

Yeh et al. [1] came up with an idea of an equiatomic alloy comprising of five elements displaying simple solid solution microstructure. Cantor et al. [2,3] simultaneously developed alloys following the same concept. This new class of metallic materials was denoted as high entropy alloys (HEA). They generated considerable interest in the scientific community, deriving their properties not from a single dominant element, but from a multiple elements arranged in a single cubic lattice. Over the time, a number of various alloy systems have been examined, exhibiting many intriguing properties, such as extremely good combination of strength and ductility [4–7], high temperature strength [8,9], wear resistance [10–12], creep [13] etc.

Considering these, it is not surprising to learn that high expectations are being put into the development of these new materials. However, most of the alloys in the presented studies derive from the original one solid solution concept (i.e., the currently acknowledged basic HEA principle) as they exhibit multiphase structures. In fact, it has been proposed by Wu et al. [14] that the idea of stabilization of a simple solid solution by the increase of configurational entropy by the addition of more elements to the alloy may be wrong. They highlighted a more

prominent role of the elements selection, also for the improvement of the extent of solid solution strengthening.

Gludovatz et al. followed this idea in their work [15]. In their attempt to improve low temperature fracture toughness of a (well-known) CrMnFeCoNi high entropy alloy, they have examined its variant using three elements only: Co, Ni, and Cr. The alloy was denoted as medium entropy alloy (MEA). Surprisingly, the CoCrNi alloy with pure face centered cubic (FCC) solid solution microstructure exhibited fracture toughness unrivalled by any other known HEA and competing with the best modern materials [15]. On top of that, strength and ductility further increased with decreasing temperatures.

Interestingly, the CoCrNi composition was previously studied by Wu et al. [14,16], too. In their work, a wide range of FCC single phase equiatomic alloys composed of three to five elements was compared. Again, the alloy exhibited the best combination of tensile strength and ductility over a wide range of tested temperatures (–196 °C to 400 °C). These properties are believed to come from the observed deformation mechanism of a dislocation slip coupled with deformation nano-twinning, resulting in the suppression of plastic instability occurrence.

The CoCrNi alloy surely exhibits an incredible ductility and fracture resistance. However, its strength may be insufficient in certain

\* Corresponding author.

E-mail address: [moravcik@fme.vutbr.cz](mailto:moravcik@fme.vutbr.cz) (I. Moravcik).

demanding structural application (especially at elevated temperatures). In such cases, its properties could be enhanced by an intended addition of a strengthening second phase, thereby forming a metal matrix composite (as in the case of e.g. ODS materials). Considering its simple solid solution nature, the alloy is particularly suitable for such MMC production. The synergic effect of its exceptional damage tolerance as a matrix and any high strength ceramic or intermetallic reinforcement could produce a composite with exceptional properties upon further development.

Until today, the alloy has been predominantly produced by metallurgical process (mainly casting) methods. These are, however, usually incapable of production of composite materials and frequently experience other associated problems, such as controlling the prospective grain size growth. In this article, a different route of CoCrNi bulk alloy fabrication via powder metallurgy route is presented: a combination of mechanical alloying (MA) for composite powders production and their subsequent densification by spark plasma sintering (SPS). In the past, such combination has been proven to be capable of production of wide array of advanced composite materials [17–21]. The alloy in the presented study was then characterized in terms of its microstructure, chemical and phase composition as well as thermo-mechanical properties, i.e. a knowledge that may serve as a basis for future design of CoCrNi-based MMC.

## 2. Experimental

The composition of the investigated alloy was CoCrNi (expressed in atomic ratio). Elemental powders of chromium, cobalt and nickel were purchased from Sigma Aldrich (purity levels of nickel and cobalt purity > 99.5 wt%, chromium > 99.0 wt%). It is important to note that as determined by a performed EDS analysis, the > 1% chromium powder impurities were mostly attributed to Al element. The powders were subsequently processed by mechanical alloying. The process was carried out in a high performance X150CrMoV 12-2 steel milling bowl. The powders were sealed together with a milling medium (a mixture of 15 mm and 20 mm hardened 100Cr6 bearing steel balls, 10:1 total ball to powder weight ratio) in a high purity nitrogen atmosphere (6.0). The sealed bowl was then inserted in a planetary ball mill (Fritsch Pulverisette 6). Milling was conducted at a speed of 250 rpm for 30 h. To remove the powder stuck to the milling balls surfaces, toluene was further added and such wet milling has been performed for additional 5 h. The powders were then removed from the milling bowl and dried in air.

The ball milled powders were subsequently consolidated by SPS technology (RHP-Technology) in a 50 mm-inner-diameter graphite die at 1180 °C for 10 min. The sintering was performed in a vacuum at a constant pressure of 30 MPa. The heating from room temperature to 1000 °C was done under the heating rate of 100 °C min<sup>-1</sup> with 20 min dwell time at temperature of 550 °C. The dwell time was included in order to remove any organic compounds potentially present in the powders (e.g., the toluene used in the milling). From 1000 °C to 1100 °C, the heating rate was reduced to 50 °C min<sup>-1</sup> and further to 20 °C min<sup>-1</sup> in the final sintering range of 1100–1180 °C to ensure the best densification conditions. After the final sintering dwell time, the pressure from pistons was released, electric current was cut-off and the set up was left to slowly cool down in the evacuated chamber. This way, cylindrical samples with 50 mm diameter and thickness of 6 mm were prepared.

From the bulk sintered compacts, several different sample types were prepared. For SEM and XRD analyses, blocks with dimensions approximately 6 × 6 × 4 mm were cut out, resin-mounted and metallographically polished. The blocks along with the initial powder feedstock as well as fractured surfaces after a mechanical testing were analyzed by SEM (Zeiss Ultra Plus) utilizing energy-dispersive X-ray spectroscopy (EDS), electron back scattered diffraction (EBSD) and electron channeling contrast imaging (ECCI) techniques. Vickers

hardness measurement was performed with a load of 300 g on polished samples (7 measurements). Additionally, thin foil specimens were prepared for TEM (Jeol 2200F) observation of microstructure and selected area electron diffraction (SAED) analysis by material grinding and precision ion polishing system (PIPS). XRD technique was used to observe the phase composition of the materials. Philips X'Pert diffractometer (40 kV) with Cu K<sub>α</sub> radiation was used for measurements. The XRD patterns were recorded in the 2θ range of 30–120°. The analysis was performed using X'Pert High Score Plus software.

Subsequently, 27 × 6 × 4 mm bars were cut out from the samples by means of EDM (electric discharge machining). From these, specimens for tensile testing were machined to obtain a cylindrical shape with a diameter of 2 mm and the gauge length of 7.6 mm. The tensile test was then performed on 3 samples with a crosshead speed of 0.2 mm min<sup>-1</sup> (strain rate of 0.25 × 10<sup>-4</sup> according to EN ISO 6892 [22]) at room temperature. The tensile tests were carried out on Zwick-Roell Z250 universal testing machine.

Additional 2 × 3 × 4 mm rectangular bar was cut out from the SPS compact for determination of room temperature elastic properties by resonant ultrasound spectroscopy (RUS) method [23,24]. RUS has been recently proved an appropriate tool for characterization of elastic constants of HEA alloys [25]. The experiments were performed using contact-less laser-ultrasound device described in details e.g. in [26]. Resonant frequencies and corresponding modal shapes of the first 20 resonant modes of free elastic vibrations of the bar were recorded. The RUS spectrum was then complemented by pulse-echo measurements of longitudinal wave velocity in the direction perpendicular to the largest face of the sample. Such a combination of ultrasonic methods enabled reliable and accurate determination of both independent elastic constants of the material, i.e. the Young's modulus *E* and the Poisson's ratio *ν*; elastic isotropy of the material was assumed. The experiments were performed in a temperature chamber (RT = (20.00 ± 0.05) °C) under dilute (30 mbar) nitrogen atmosphere.

Finally, a thermo-mechanical analysis (TMA) by a measurement of sample one directional size change with heating and cooling rates of 5 °C min<sup>-1</sup> from 20 °C to 1100 °C has been performed for the observation of phase changes and measurement of coefficient of thermal expansion (CTE) respectively.

## 3. Results and discussion

### 3.1. Phase and microstructural evolution

The results of XRD phase analyses are presented in Fig. 1. The diffraction patterns of Co, Ni and Cr elements are presented in the patterns corresponding to pre-mixed powders in Fig. 1a. Note that the peaks of hexagonal Co elements were somewhat weaker as compared to the others.

In the pattern attributed to the state of the powder after the MA process (Fig. 1b) peaks corresponding to three different phases were observed. The dominant phase was an FCC Ni-based solid solution with the lattice parameter of 3.532 Å and a calculated volume fraction of 51.2%. The second and third phases are Cr-like BCC solid solution with 2.884 Å and volume fraction of 29.2%, and Co-like HCP phase with *a* = 2.487 Å and *c* = 4.132 Å comprising 19.6 vol% of the microstructure, respectively. These phases are referred to as solid solutions due to peak shift to higher angles (cf. pure elements), caused by a partial dissolution of the other two elements. All the peaks are significantly broadened as compared to the state before the milling. This is the result of either the elastic strain present in the powder, or the crystallite size refinement. Both phenomena would suggest that the lattices of the powder particles are severely distorted and of high dislocation density as the result of the plastic deformation introduced to the powders during MA. Given its multi-phase structure, the alloying process in the alloy probably has not been completely finished after the milling. Nevertheless, the powders were mechanically activated to promote accelerated sintering (i.e.,

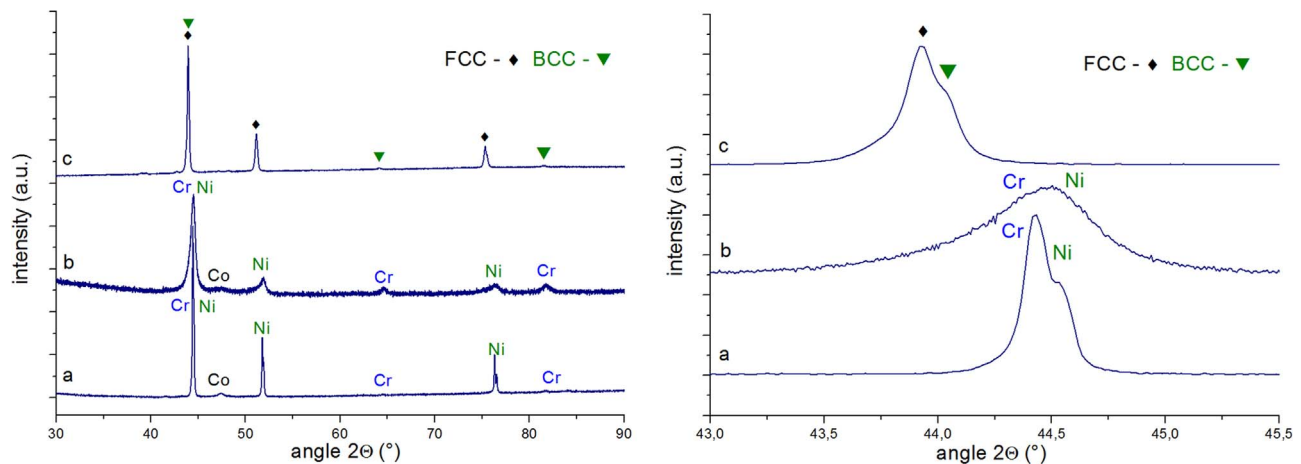


Fig. 1. XRD patterns of the materials at different stages of the preparation process: a) premixed as-received powders b) powders after milling procedure c) SPS compacted bulk material. Right graph presents magnified 43–45.5° range.

their diffusivity was increased due to a higher dislocation density and higher grain boundary area). This was later confirmed by a successful formation of a homogeneous microstructure after the SPS consolidation at high temperatures through enhanced diffusion rates.

After the high temperature sintering, a considerable change in the phase composition has been observed, with patterns of two phases present in the microstructure (Fig. 1c). The major phase was an FCC solid solution with lattice parameter of 3.565 Å comprising 94.4% of the bulk microstructure, while the minor phase was a BCC solid solution with 2.895 Å lattice parameter and 5.6% fraction. The peaks of the phases are much sharper and thinner as a consequence of bigger crystallite sizes. Such increase may have been triggered by the used high temperatures that promote grain size growth. The Co-based HCP phase was not detected in the XRD pattern. The change in lattice parameters (and the resulting peak shift seen in Fig. 1 close up figure) is attributed to the Co element dissolution.

The chemical composition of the sintered bulk alloy identified by EDS analysis (Table 1) almost perfectly matched the desired calculated composition. The detected presence of iron is attributed to the wear of the steel milling balls during the high energy milling process, where chipped micro-shards of the steel may have become embedded into the powder particles prior to sintering. Due to its negligible volume (0.7 at %) and the similarity of iron atoms (atomic number 26) to chromium (24), such contamination should not influence the resulting microstructure and properties of the alloy.

The morphology and cross section features of the powder particles after the milling procedure are illustrated in Fig. 2. In the powders cross section, the fine layered microstructure of alternating elements (or their respective solid solutions) can be observed in accordance with the XRD results. The thickness of most of the layers is in the range of hundreds of nanometers (illustrated by EDS mapping presented in Fig. 2d). Upon subsequent high temperature sintering, such extensively mechanically activated microstructure should provide sufficiently short diffusion paths for the mutual reaction of the present elements i.e. formation of microstructure without the traces of original particles. After prolonged milling, the layered microstructure would disappear – full solid solution would be obtained, however at the cost of much more significant iron contamination as a result of more extensive wear of steel milling balls.

Table 1  
Chemical composition of the produced materials (EDS, atomic %).

Element	Ni	Co	Fe	Cr
Desired composition	33.3	33.3	0	33.3
Bulk after SPS	33.2	32.2	0.7	33.5

Fig. 3 shows SEM micrographs of the bulk alloy compacted via SPS. No porosity is present throughout the whole cross-section and no traces of the original particle boundaries or layers of different phases that were present in the powder particles before the SPS densification can be seen. In accordance with the XRD measurements, the microstructure was identified as consisting of grains of a FCC phase and a minor secondary phase. The latter should correspond to the BCC phase and it was observed solely at the individual grain boundaries, as denoted by red arrows in Fig. 3. Considering these, it is suggested herein that it formed through a secondary precipitation process from the initially formed FCC phase during the cooling from the sintering temperatures. The dark contrast spherical phase present in the microstructure (denoted by yellow arrows in Fig. 3b with corresponding EDS microanalysis in Fig. 3c) was identified by EDS analyses of both SEM and TEM samples as aluminum and chromium oxide inclusions; considering aluminum's and chromium's high affinity towards oxygen, it may have formed as a result of powders contamination due to air exposure of the elemental powders prior to and after the milling procedure. The presence of aluminum oxides is attributed to negligible aluminum content in feedstock chromium powders, most probably as a result of the powder manufacturing procedure.

Fig. 4 represents a microstructure of the bulk alloy as observed by TEM. Planar dislocation arrays in FCC grains are visible in Fig. 4a (denoted by red arrow). A dislocation network formed by dislocation pinning at the present nano-scale oxides dispersion is visible in Fig. 4b, suggesting a strong dispersion strengthening effect. Additionally, another notable microstructure feature was observed in the TEM imaging (denoted by yellow arrow in Fig. 4b). Considering its properties, the feature may represent the parallelepiped stacking fault, as also observed previously by Zhang in CoCrFeMnNi high entropy alloy [27]. This volume structural defect is supposedly formed by the simultaneous movement of partial dislocations on two active {111} planes and their subsequent intersection, forming an obstacle around which entangling of dislocations occurs. This defect structure is retarding the dislocation movement, and thereby increasing the strength and strain hardening capacity of the alloy [27]. The presence of several stacking faults has been observed within the FCC grains, as denoted by green arrows in Fig. 4c.

In Fig. 5, the intergranular secondary phase precipitate is visible (denoted by green arrow) at the boundaries of the major FCC phase grains. The selected area diffraction pattern analysis of the figure (presented in Fig. 5b) revealed the phase bearing a BCC crystal lattice. The phase possesses chemical composition of almost pure Cr element, as observed by the point EDS measurement and corresponding elemental mapping in Fig. 5c. Therefore it perfectly corresponds to the Cr based BCC phase revealed previously by XRD and SEM analyses.

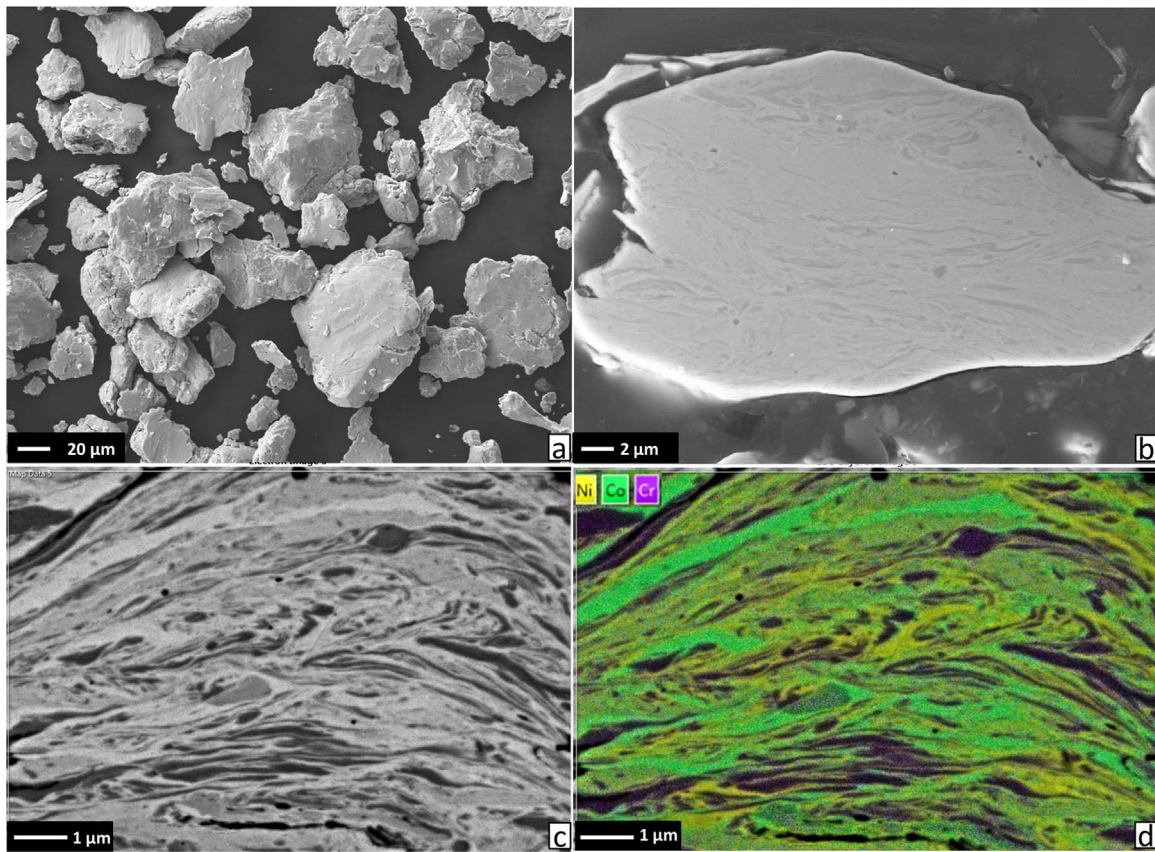


Fig. 2. SEM back scattered electrons micrographs of the milled powder particles used for SPS: a) morphology b) cross section image of the powders c) cross sectional powder microstructure d) corresponding EDS map revealing extremely fine layered microstructure.

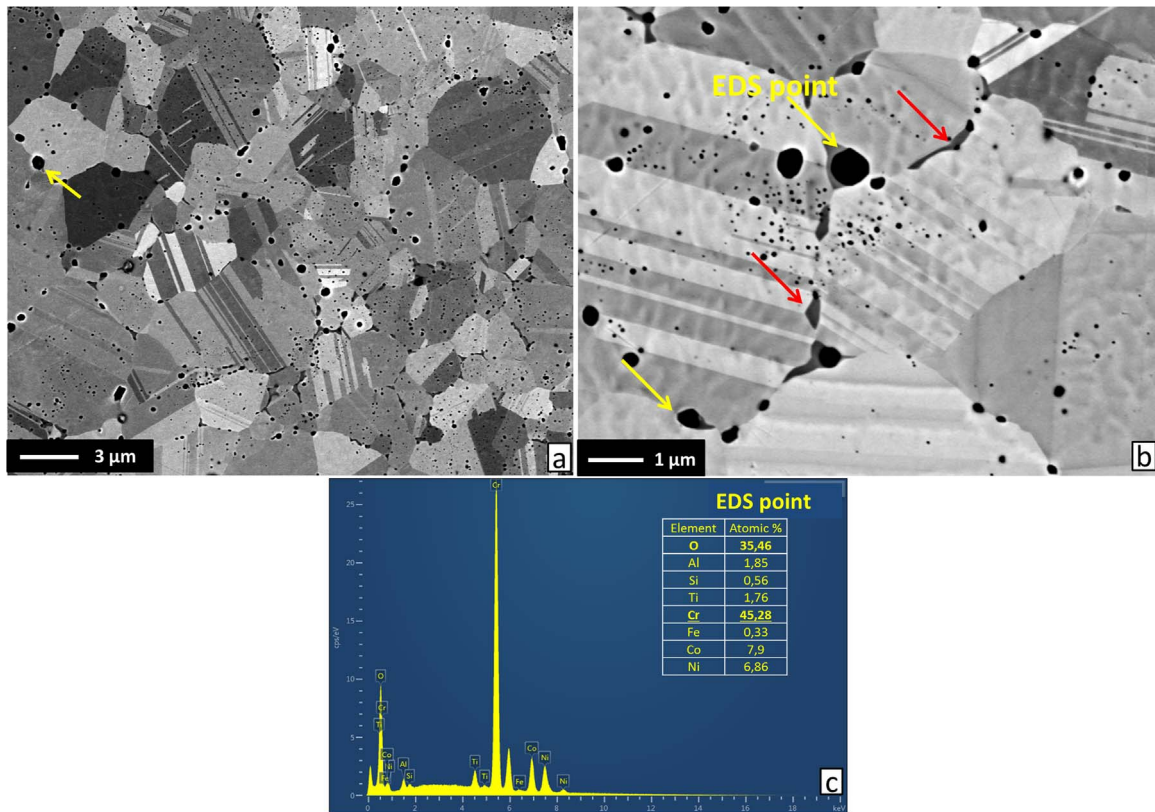


Fig. 3. SEM back scattered electrons micrographs of the SPS sintered bulks revealing a) polycrystalline fine-twinned FCC microstructure and b) second BCC phase (denoted by red arrows). The dark contrast dots (yellow arrows) were identified as chromium and aluminum oxide particles by EDS c) corresponding EDS pattern of denoted oxide particle. (For interpretation of the references to color in this figure legend, the reader is referred to the web version of this article.).

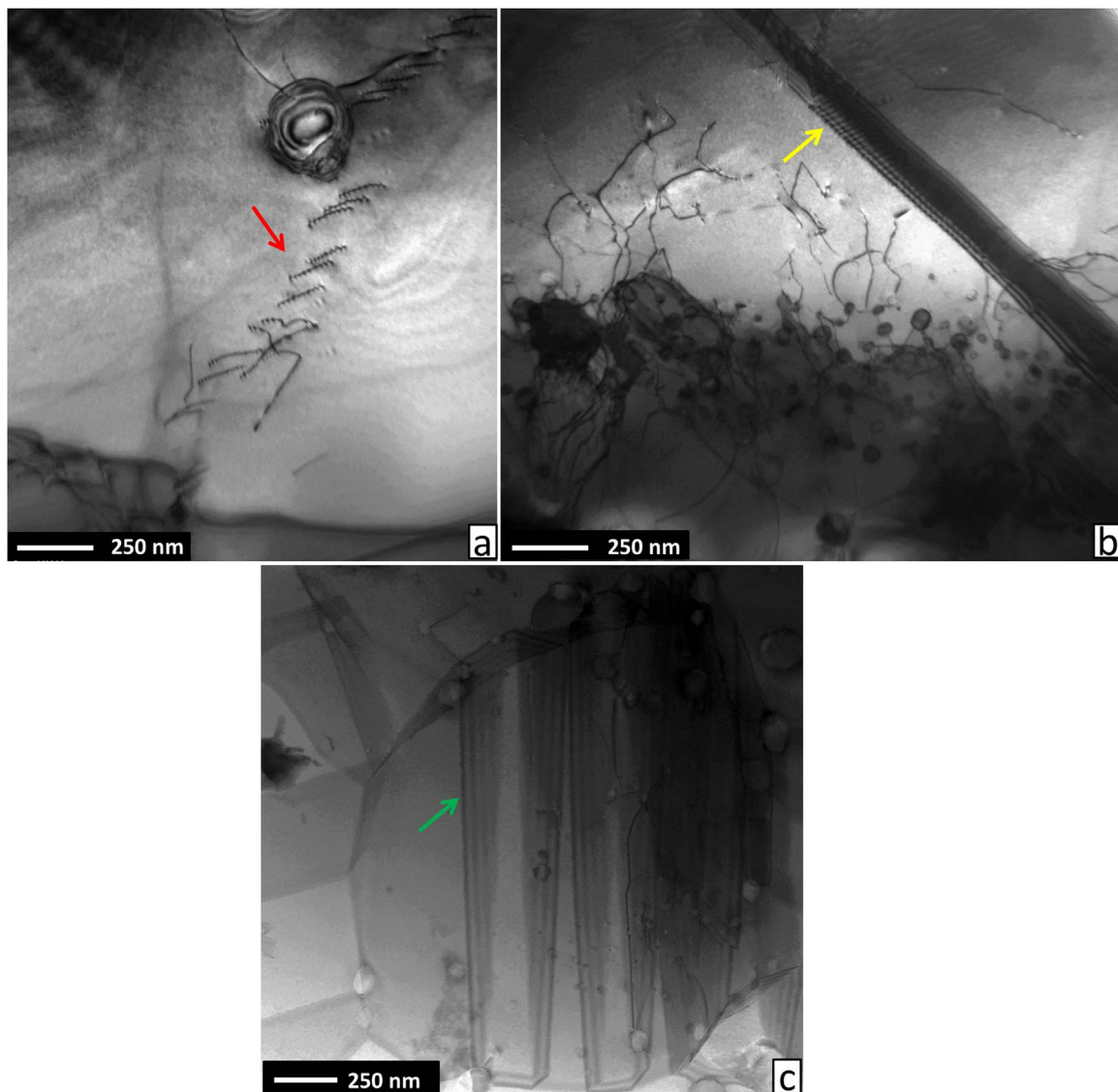


Fig. 4. TEM micrographs of a) FCC grains containing dislocation arrays (red arrow) b) dislocation networks pinned by oxide particles and stacking-fault parallelepiped structure (denoted by yellow arrow) formed by slip on multiple  $\{111\}$  planes c) FCC grain containing several stacking faults denoted by green arrow. (For interpretation of the references to color in this figure legend, the reader is referred to the web version of this article.)

The fact that the sintered compacts are composed of a two-phases mixture (supported by XRD, SEM and TEM studies) is in a contradiction to the previous results, where this alloy was shown as bearing single FCC phase only [14–16]. Importantly, the produced alloy is in a thermally stable state (as was proven by a subsequent TMA analysis). As such, the phase content discrepancy (cf. e.g. Gludovatz et al. [14]) is most probably associated with the different manufacturing process. The materials in the previous studies were produced by a casting route, followed by a subsequent homogenization and rolling to obtain homogenous microstructures. After the homogenization, water quenching from high temperatures was utilized. Therefore, the associated cooling rates were much higher as compared to the presented material produced by SPS (slow cooling in a graphite die under vacuum inside the SPS chamber) and may have resulted into a formation of metastable compounds. Further to that, in the study by Wu et al. [14] it is proposed that from the predictions based on phase diagrams, the alloy should bear single phase FCC microstructure only in the temperature interval 927–1227 °C. Below 927 °C, the alloy should be composed of a multiphase microstructure. In fact, the study actually proposed that some of the studied FCC alloys might in fact still be in non-equilibrium conditions and could decompose to form more

complicated structures upon long time annealing. Given these and the outcomes of the study presented herein, it is suggested that the widely accepted opinion of this alloy being of single phase nature may not be valid in general, but may depend on the used fabrication method instead. To build on the currently obtained results and yield additional knowledge on this issue, expanded study of the investigated alloy microstructure and properties is undergoing at the moment.

The EBSD orientation maps (Fig. 6a) and pole maps (Fig. 6c) suggest that, despite the uniaxial pressing during the sintering process, there was no apparent preferred orientation of the FCC phase grains. Aside from others, this finding justifies the assumption of the isotropic elastic behavior applied in the subsequent RUS measurements. Due to the resolution constraints of EBSD, the secondary BCC phase was not detected. The average grain size determined from the orientation map was 4.11  $\mu\text{m}$ . However, as can be seen from grain size distribution histogram presented in Fig. 6b, the grain size distribution is relatively non-uniform: almost 85% of grains have diameters smaller than 2  $\mu\text{m}$ , while bigger grains over 8  $\mu\text{m}$  represent less than 1% of the total grains quantity only. A high density of annealing twins was found within the FCC grains, suggesting that the alloy has a low stacking fault energy in the interval of  $18 < \gamma_{\text{SFE}} < 45 \text{ MJ m}^{-2}$  [28].

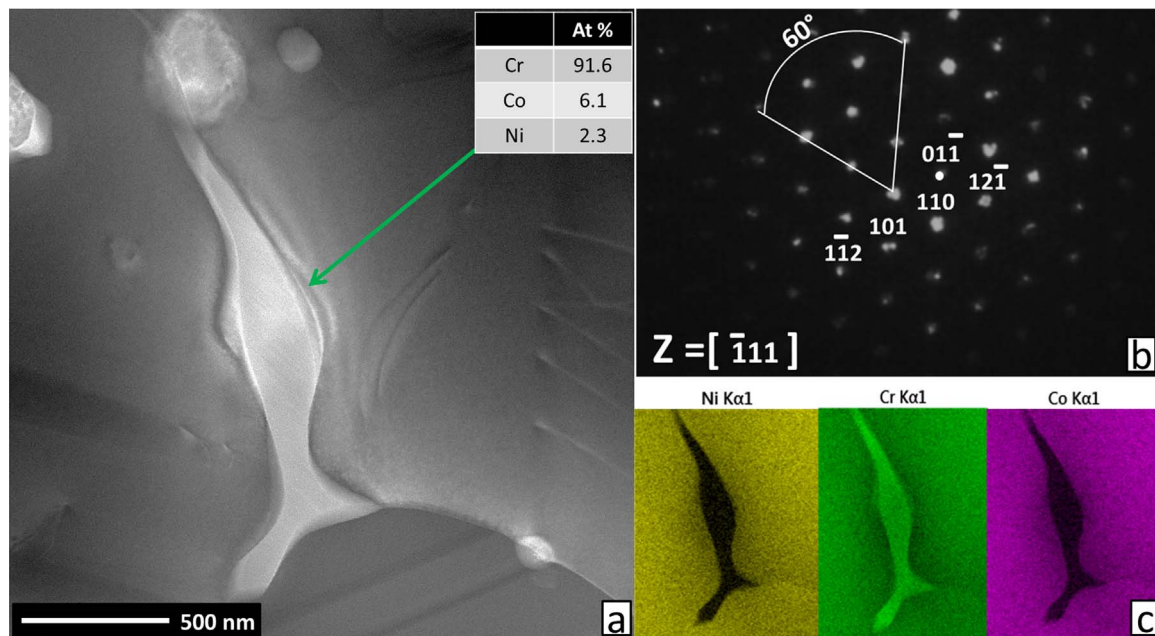


Fig. 5. TEM analysis of secondary phase that precipitated at FCC grain boundaries a) TEM micrograph of the precipitate (denoted by green arrow) with corresponding point EDS composition measurement b) corresponding SAED pattern revealing BCC lattice c) EDS elemental distribution maps. (For interpretation of the references to color in this figure legend, the reader is referred to the web version of this article.).

### 3.2. Mechanical behavior

The measured hardness of the alloy reached 309 HV0.3, i.e. a value relatively high for almost pure (94.4%) FCC material without involving any strengthening process (such as e.g. work hardening) prior to testing.

The tensile properties are summarized in Table 2. The alloy exhibited tensile yield strength of  $\sigma_{0.2} = 652$  MPa, ultimate tensile strength of UTS = 1024 MPa, and tensile elongation to fracture  $E_t = 25.9\%$ , suggesting an excellent strain hardening ability. The extremely small data scatter stems from the homogeneous structure of the SPSed compacts. From the representative engineering stress - engineering strain tensile curve (Fig. 7), a uniform deformation behavior without necking has been observed.

The comparison of these results with available data from literature is presented in Table 3. It can be seen that the produced PM alloy exceeds its cast counterparts in both yield and ultimate tensile strength values, but is lacking in tensile elongation to fracture. At this moment, it should be noted that the mechanical properties taken from the previous research studies [15,16] are considered as one of the best currently available results, well exceeding the results of most of other comparable materials [29,30]. The properties of the PM alloy presented in this study could be attributed to several factors, as explained below.

The improved strength properties could be the results of grain boundary strengthening of comparatively finer grain size, a consequence of the utilized PM manufacturing process. Another phenomenon contributing to the improvement in strength is most probably strengthening by the small fraction of the secondary BCC phase and fine oxide inclusions. The decreased tensile elongation to fracture is most probably the consequence of lower strain hardening capacity and detrimental effect of coarser oxide inclusions, acting as nucleation sites for void formation.

The fracture surfaces of the broken tensile test specimens were observed in SEM (Fig. 8). The fracture started approximately in the geometrical middle of the tensile specimens and ended with shear tearing at the specimen edges. The fracture surfaces exhibited a typical ductile fracture mode, a consequence of a nucleation, growth and coalescence of fine microvoids. Oxide particles were located in the middle of majority of the ductile dimples and presented the microvoids nucleation

sites (as illustrated by red arrow in inset of Fig. 8b).

The longitudinal tensile test specimen cross-section images in Fig. 8c-d (perpendicular to fracture surfaces), suggest that the plastic deformation in the alloy is carried out by a combination of dislocation slip and a deformation nano-twinning as an additional mechanism. This is apparent from the presence of dislocation cell structures (denoted by green arrow in Fig. 8c) and extremely fine deformation nano-twins visible in Fig. 8c-d – yellow arrow. Detailed HR EBSD analysis of deformation nano-twinning is provided separately in Fig. 9. As can be seen from the image, twinning has been activated on several intersecting planes (intersecting twins) in grains possessing suitable crystallographic orientation. Our observation of deformation nano-twinning is in a good agreement with the previous findings obtained on cast materials [15]. The study suggested that, of the two mechanisms, the deformation nano-twinning is the main factor causing the alloy's exceptional combination of strength and ductility. Further to that, the simultaneous improvement of both characteristics in the cryogenic temperature range is attributed to a shift from the dislocation slip to the deformation nano-twinning [15]. Incidentally, the deformation twinning mechanism is also exploited in TWIP steels (twinning-induced plasticity), one of the most damage tolerant materials with extremely high ductility [30,31].

In order to characterise the plastic deformation mechanism of the produced material in detail, its work hardening performance has been qualified. To do so, the strain hardening exponent was assessed by fitting the true stress- true strain curve ( $\sigma_{tr} - \epsilon_{tr}$ ) by the modified Hollomon equation [32]:

$$\ln(\sigma_{tr}) = \ln(K) + n \ln(\epsilon_{tr}) \quad (1)$$

where  $K$  is a material constant and  $n$  is the strain hardening exponent. The original measured raw data without any pre-processing were used for the analysis. The result of this analysis is presented in Fig. 10a, where  $n$  is presented as a slope of the calculated  $\ln(\sigma_{tr}) - \ln(\epsilon_{tr})$  curve in the first stage of plastic deformation, before reaching fracture conditions. The exponent values showed a smooth change from 0.1 to 0.28. The higher the  $n$  value is, the higher is the strain hardening of a material in general. This contributes to the material overall ductility by retarding the onset of localized plastic deformation, thus postponing the appearance of plastic instability (necking) [28,32]. To further evaluate

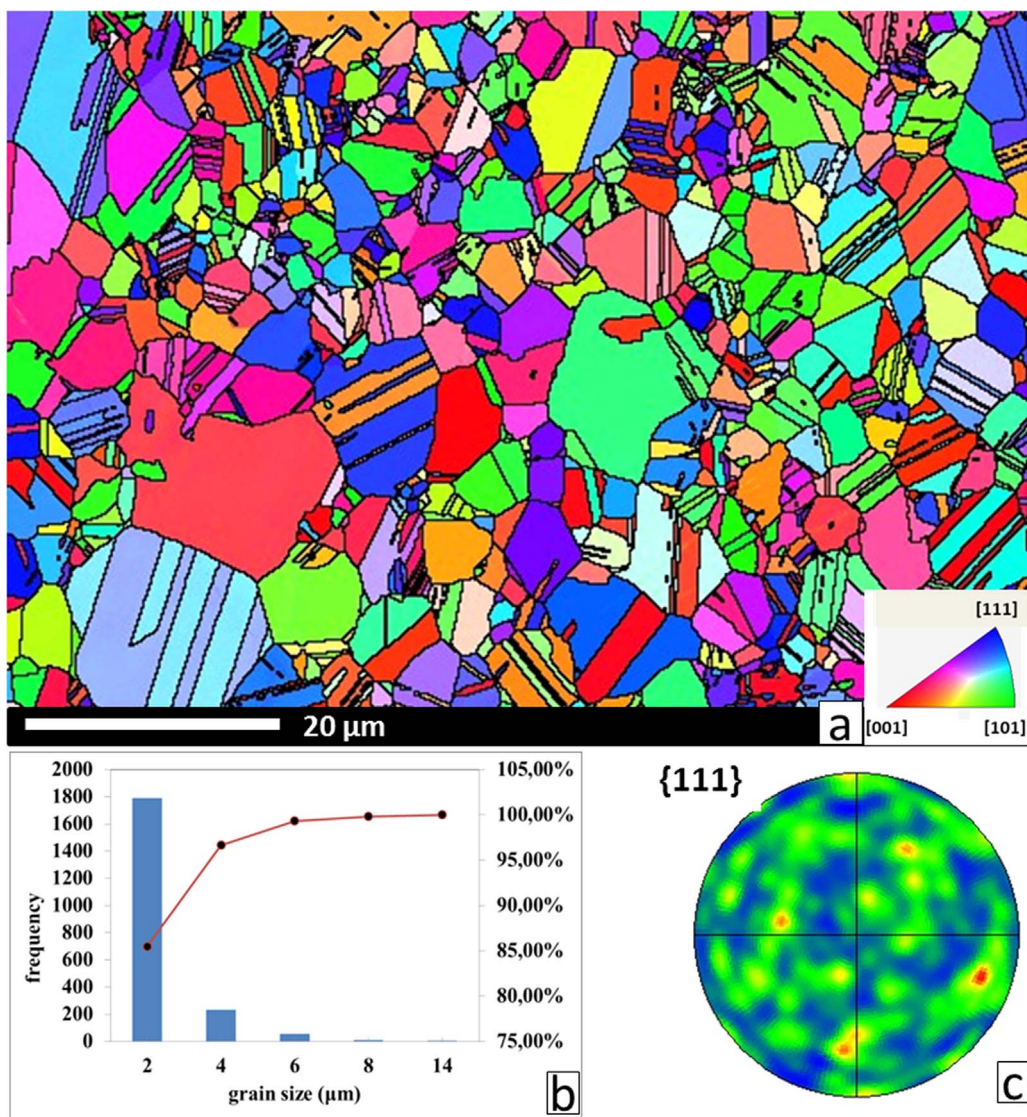


Fig. 6. EBSD analysis of SPS sintered bulk material; a) microstructure orientation maps with visible annealing twins b) calculated grain size distribution curve c) pole maps showing no significant preferred orientation of its grains.

Table 2  
Tensile test results of investigated alloy after SPS.

$\sigma_{0.2}$ [MPa]	UTS [MPa]	Elongation to fracture [%]	Reduction [%]	Work of fracture [ $J\ cm^{-3}$ ]
$652 \pm 0.58$	$1024 \pm 5.77$	$25.9 \pm 0.7$	$21.5 \pm 1.41$	246

this phenomenon, the strain hardening rate ( $d\sigma_{tr}/de_{tr}$ ) was calculated and plotted against on a true strain  $\epsilon_{tr}$  (Fig. 10b). The strain hardening rate changed smoothly, without any sudden discontinuities – suggesting no sudden change in deformation mechanism. Based on the fact that the deformation in the CoCrNi alloy is in later stages carried out by a combination of the dislocation slip and deformation nano-twinning (as seen in Fig. 8), both deformation mechanism are most probably employed simultaneously, depending on the grain orientation.

In the work by Pierce [31], the influence of stacking fault energy  $\gamma_{SFE}$  on changes in the deformation mechanism in advanced steels was studied. The authors found out that with the  $\gamma_{SFE}$  of  $15\ MJ\ m^{-2}$ , the deformation mechanism consisted of FCC to  $\epsilon$  (HCP martensite) strain induced phase transformation as well as a planar dislocation glide, while a combination of mechanical nano-twinning and dislocation cross slip occurred in the alloy at  $\gamma_{SFE} = 39\ MJ\ m^{-2}$ . Interestingly, the shape of the ( $d\sigma_{tr}/de_{tr}$ ) curve of CoCrNi PM alloy in this study also follows the

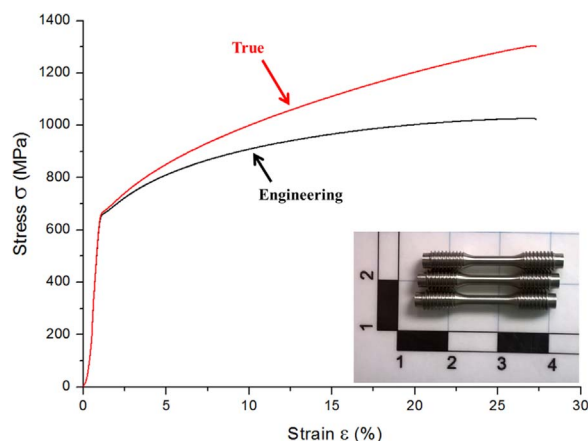


Fig. 7. Representative tensile test stress – engineering strain curve for room temperature. Geometrical features of the tensile specimens are provided in the inset.

curve corresponding to the  $\gamma_{SFE}$  of  $39\ MJ\ m^{-2}$ . Therefore, there should be no strain induced phase transformation in the produced CoCrNi alloy and its deformation mechanism should comprise of cross slip and deformation twinning. The theory of the prevalence of the dislocation cross slip over the planar gliding mechanism is also supported by the

**Table 3**  
Tensile test results comparison of investigated material with previous studies of cast materials.

$\sigma_{0.2}$ [MPa]	UTS [MPa]	Elongation to fracture [%]	Preparation method	Reference
652	1024	25.9	Milling + SPS	this work
320	880	60	Casting + homogenization + deformation	[16]
440	890	72.5	Casting + homogenization + deformation	[15]

fact that a dislocation cell structure is formed (Fig. 8c) due to ability of the dislocations to change direction in the planes [33], rather than a formation of straight lines of highly dense dislocation walls (HDDW), that are present in the microstructure where planar dislocation glide is preferred [34].

### 3.3. Elastic constants

From the resonant ultrasound spectroscopy measurements (RUS), the values of elastic constants  $E = (222 \pm 2)$  GPa and  $\nu = (0.30 \pm 0.01)$  were obtained. The value of Young's modulus  $E$  is very close to but slightly lower than 229 GPa reported by Gludovatz et al. [15] for the room temperature. It is interesting that the obtained Young's modulus is very close to Hill's average  $E = 227$  GPa for a 1: 1: 1 mixture of pure Co, Cr, and Ni polycrystals, taking  $E = 204$  GPa for

cobalt [35],  $E = 210$  GPa for nickel [35] and  $E = 272$  GPa for annealed chromium [36]. Also the Poisson's ratio obtained by the RUS measurement is in agreement with Gludovatz et al. [15]. Hence, it can be concluded that the elastic properties of the cast material and of our material prepared by powder metallurgy are fully comparable.

### 3.4. Thermomechanical behavior

The results of relative size change measurements are presented in Fig. 11. As could be seen, the produced alloy exhibited almost linear size change dependence with temperature. The measured CTE had a value of  $17.4 \times 10^{-6} \text{ K}^{-1}$  (cf. the value of  $10.44 \times 10^{-6} \text{ K}^{-1}$  calculated as an average value of Co, Cr and Ni elements). The discrepancy of the two figures might stem from the fact that in the alloy, the three elements are arranged in one FCC solid solution (plus minor BCC phase content), while the original elements lattices might differ (BCC Cr, HCP Co).

The measured value is relatively high as compared to present-day alloys of comparable density, that generally exhibit values of CTE ranging from  $8$  to  $14 \times 10^{-6} \text{ K}^{-1}$  [37]. In fact, the high CTE value of the alloy presents a unique possibility of the alloy to be used as a matrix in ceramic reinforcements MMC applications. As the CTE of ceramic materials is usually low, in the range of  $4$ – $10 \times 10^{-6} \text{ K}^{-1}$ , the combination of CoCrNi MEA matrix with such reinforcements would yield a significant strengthening effect through high residual stresses development at the phase interfaces. The stress development due to the significant CTE mismatch is generally associated with a formation of geometrically necessary dislocations (GND) during cooling from

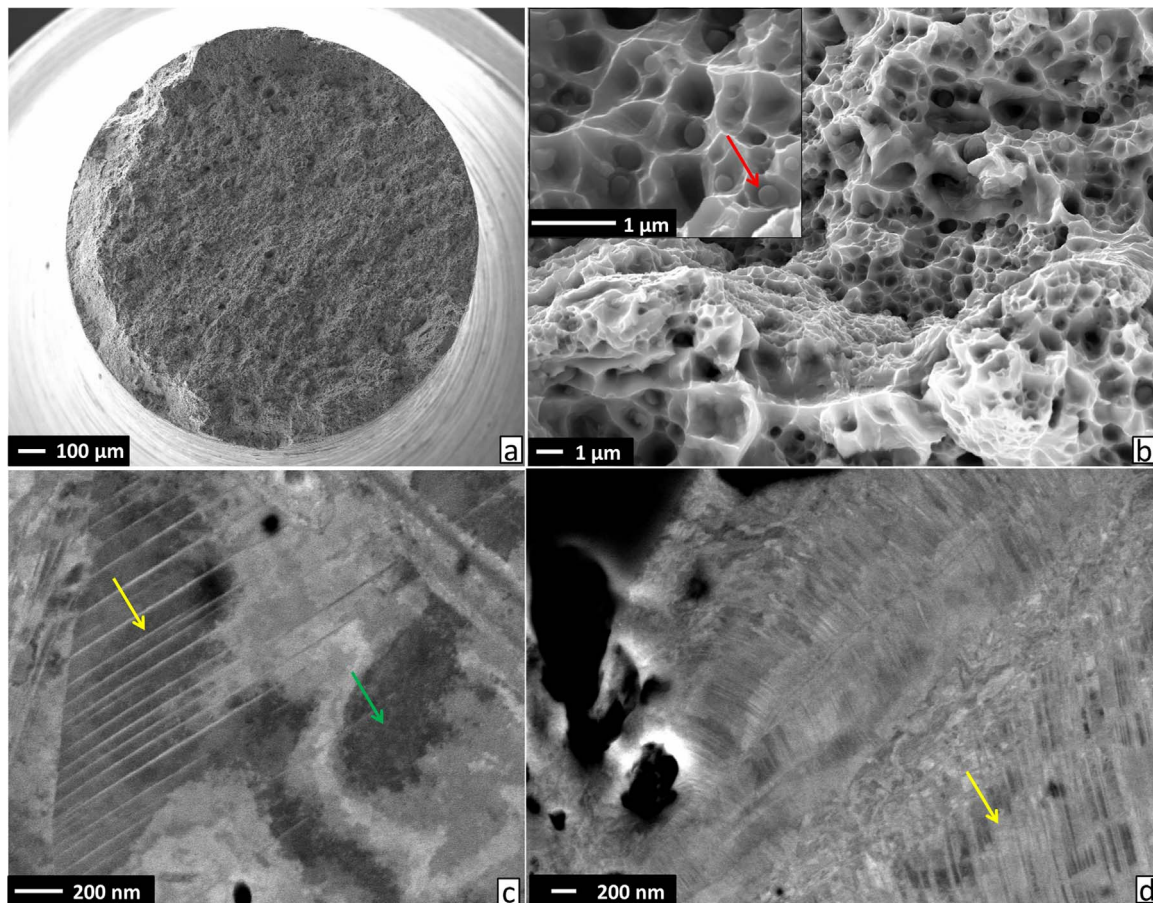


**Fig. 8.** SEM micrographs of a) tensile test specimen fracture surface overview with apparent shear edges b) ductile fracture dimples present at the fracture surface and the oxide inclusions frequently observed at the dimple bottom (red arrow) c, d) polished longitudinal cross-section perpendicular to tensile axis directly under fractured surface of tensile specimen. Formed dislocation cells are denoted by green arrow and the deformation twins by yellow arrow. (For interpretation of the references to color in this figure legend, the reader is referred to the web version of this article.)

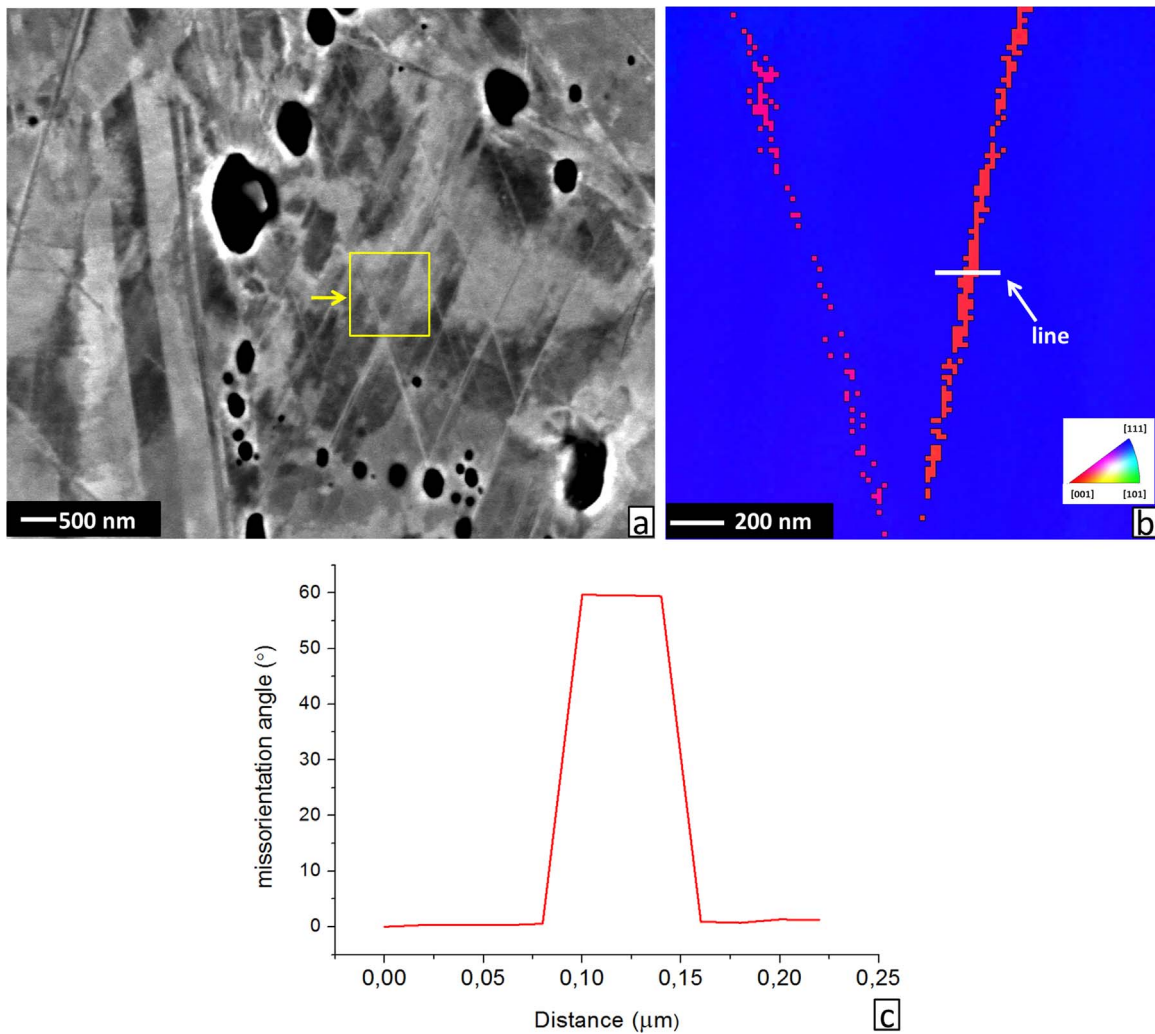


Fig. 9. deformation nano-twinning analysis under fractured surface of tensile specimen a) SEM ECCI image of twinned grain with area subjected to HR EBSD analysis denoted by yellow square b) orientation map of corresponding yellow square area c) corresponding misorientation as a function of distance for the white line. (For interpretation of the references to color in this figure legend, the reader is referred to the web version of this article.)

processing temperatures [38]. The prospect of using the produced alloy in the MMC application is further supported by the fact that there were no peaks or discontinuities on the measured size change curve, suggesting an absence of any phase transformation during the temperature change, thereby confirming stability of the produced alloy – this

presents one of the most important criteria for MMC matrix materials.

### 3.5. Comparison with analogous alloy systems

A direct comparison of the ultimate tensile strength and total

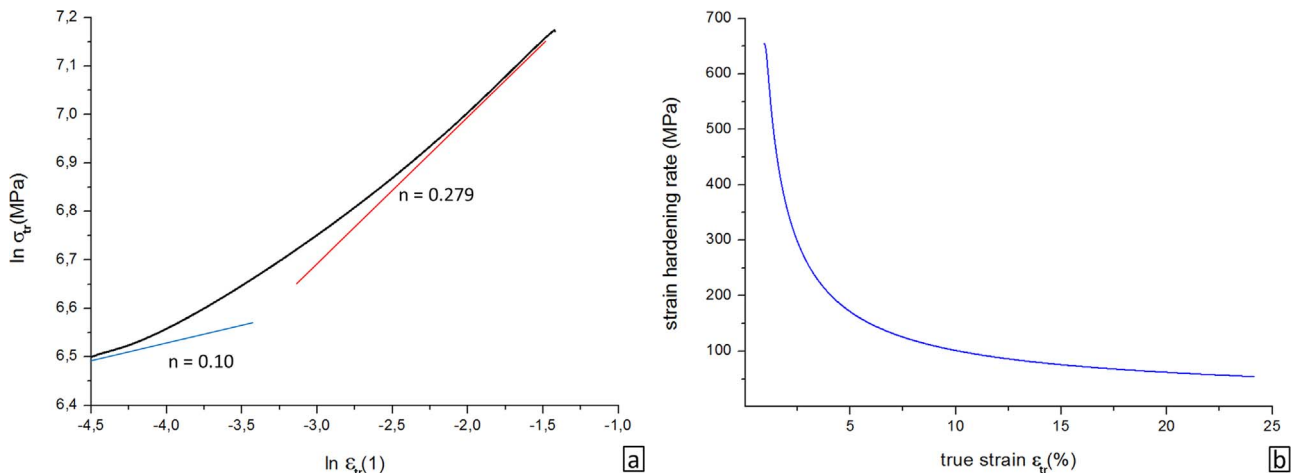


Fig. 10. Plastic behavior of the CoCrNi PM alloy characterized by a) the variation of the strain hardening exponent  $n$  determined for uniform plastic deformation stage b) strain hardening rate changes.

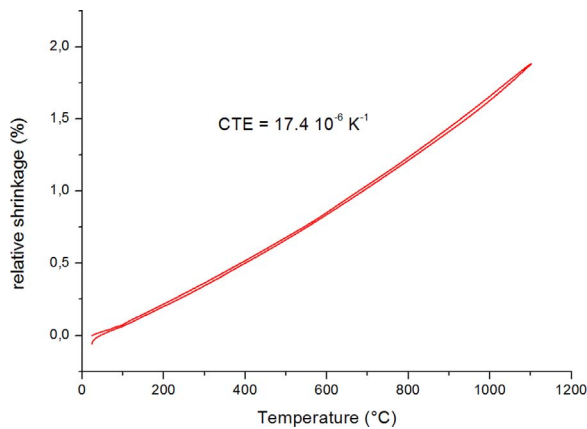


Fig. 11. TMA measurement of the prepared bulk material showing almost linear size change with changing temperature.

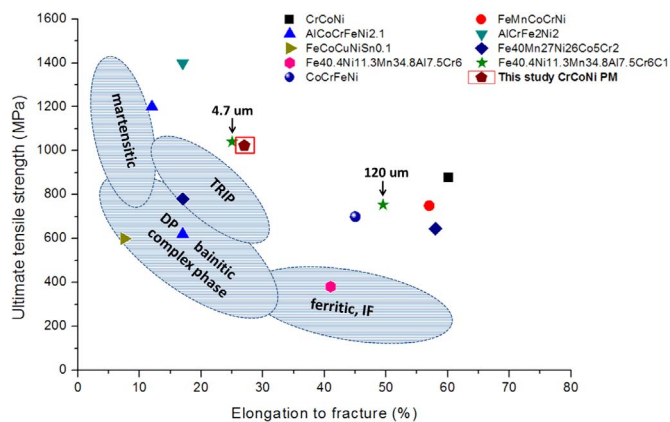


Fig. 12. Comparison of strength vs deformation of conventional materials, high and medium entropy alloys.

elongation of the current PM CoCrNi alloy with those of high strength steels and other HEA (data from references [4,16,39–45]) is presented as Ashby type plot in Fig. 12. The produced PM material exhibited a good combination of mechanical properties, competitive with other HEA that were produced by casting and subsequent deformation processes. It is worth mentioning that despite being relatively new group of materials, the high and medium entropy alloys already outperform their other additional properties (most notably corrosion resistance and wear resistance, as mentioned previously). In HEA scientific community, the fact that the final alloy properties are not only influenced by the used chemical composition, but also by the processing conditions is sometimes neglected. For instance, the  $\text{Fe}_{40.4}\text{Ni}_{11.3}\text{Mn}_{34.8}\text{Al}_{7.5}\text{Cr}_6\text{C}_1$  alloy in the study [42] properties were shown to be affected a by the grain size, which was adjusted by cold deformation from initial 120  $\mu\text{m}$  to 4.7  $\mu\text{m}$ . In the case of wrought materials, the only way to induce grain refinement is a use of deformation processes with severe cross-section reductions. Using the combination of MA and SPS presented in this paper, the materials can be produced already bearing a fine grain size (4.11  $\mu\text{m}$  directly after SPS) without the need of plastic deformation or additional heat treatment processes.

#### 4. Conclusions

In this study, CoCrNi alloy has been produced by powder metallurgy route of mechanical milling and spark plasma sintering. Microstructural parameters, mechanical and physical properties have been characterized with following results:

- the produced alloy possesses a two phase microstructure (with dominant FCC phase), as opposed to single phase alloys produced by the casting route, most probably as a results of different cooling kinetics.
- the alloy's multi-phase fine grained microstructure results in a high tensile yield strength of 652 MPa, ultimate tensile strength of 1024 MPa, tensile elongation to fracture 25.9%, and elastic modulus of 222 GPa, i.e. values superior to e.g. martensitic or TRIP steels.
- the plastic deformation is presumably not carried out by a planar dislocation glide, but rather by a combination of dislocation cross slip and deformation twinning mechanisms.
- the microstructure of the CoCrNi alloy is thermally stable and possesses a relatively high CTE of  $17.4 \cdot 10^{-6} \text{ K}^{-1}$ , yielding it a promising stable matrix material for MMC composites.

#### Acknowledgments

The research was co-funded by the Ministry of Education, Youth and Sports within the “National Sustainability Programme I” (NETME CENTRE PLUS - LO1202). Support to Czech Science Foundation project GACR 23964S is further acknowledged. The authors would like to thank Jan Cupera for his help with SEM analysis, Zdenek Spetz for his contribution to XRD analyses, Jozef Zapletal for tensile test measurements, and Vaclav Pouchly for TMA.

#### References

- [1] J.W. Yeh, S.K. Chen, S.J. Lin, J.Y. Gan, T.S. Chin, T.T. Shun, C.H. Tsau, S.Y. Chang, Nanostructured high-entropy alloys with multiple principal elements: novel alloy design concepts and outcomes, *Adv. Eng. Mater.* 6 (2004) 299–303, <http://dx.doi.org/10.1002/adem.200300567>.
- [2] B. Cantor, I.T.H. Chang, P. Knight, A.J.B. Vincent, Microstructural development in equiatomic multicomponent alloys, *Mater. Sci. Eng.: A* 375–377 (2004) 213–218, <http://dx.doi.org/10.1016/j.msea.2003.10.257>.
- [3] O.N. Senkov, G.B. Wilks, J.M. Scott, D.B. Miracle, Mechanical properties of Nb<sub>25</sub>Mo<sub>25</sub>Ta<sub>25</sub>W<sub>25</sub> and V<sub>20</sub>Nb<sub>20</sub>Mo<sub>20</sub>Ta<sub>20</sub>W<sub>20</sub> refractory high entropy alloys, *Intermetallics* 19 (2011) 698–706, <http://dx.doi.org/10.1016/j.intermet.2011.01.004>.
- [4] Y. Dong, X. Gao, Y. Lu, T. Wang, T. Li, A multi-component AlCrFe<sub>2</sub>Ni<sub>2</sub> alloy with excellent mechanical properties, *Mater. Lett.* 169 (2016) 62–64, <http://dx.doi.org/10.1016/j.matlet.2016.01.096>.
- [5] W. Chen, Z. Fu, S. Fang, Y. Wang, H. Xiao, D. Zhu, Processing, microstructure and properties of Al<sub>0.6</sub>CoNiFeTi<sub>0.4</sub> high entropy alloy with nanoscale twins, *Mater. Sci. Eng.: A* 565 (2013) 439–444, <http://dx.doi.org/10.1016/j.msea.2012.12.072>.
- [6] D. Li, Y. Zhang, The ultrahigh charpy impact toughness of forged AlxCoCrFeNi high entropy alloys at room and cryogenic temperatures, *Intermetallics* 70 (2016) 24–28, <http://dx.doi.org/10.1016/j.intermet.2015.11.002>.
- [7] I. Moravcik, J. Cizek, J. Zapletal, Z. Kovacova, J. Vesely, P. Minarik, M. Kitzmantel, E. Neubauer, I. Dlouhy, Microstructure and mechanical properties of Ni<sub>1.5</sub>Co<sub>1.5</sub>CrFeTi<sub>0.5</sub> high entropy alloy fabricated by mechanical alloying and spark plasma sintering, *Mater. Des.* 119 (2017) 141–150, <http://dx.doi.org/10.1016/j.matdes.2017.01.036>.
- [8] H.M. Daoud, A.M. Manzoni, N. Wanderka, U. Glatzel, High-temperature tensile strength of Al<sub>10</sub>Co<sub>25</sub>Cr<sub>8</sub>Fe<sub>15</sub>Ni<sub>36</sub>Ti<sub>6</sub> compositionally complex alloy (high-entropy alloy), *JOM* 67 (2015) 2271–2277, <http://dx.doi.org/10.1007/s11837-015-1484-7>.
- [9] M.A. Manzoni, S. Singh, M.H. Daoud, R. Popp, R. Völkl, U. Glatzel, N. Wanderka, On the path to optimizing the Al-Co-Cr-Cu-Fe-Ni-Ti high entropy alloy family for high temperature applications, *Entropy* (2016) (<http://dx.doi.org/1810.3390/e18040104>).
- [10] P.K. Huang, J.W. Yeh, T.T. Shun, S.K. Chen, Multi-principal-element alloys with improved oxidation and wear resistance for thermal spray coating, *Adv. Eng. Mater.* 6 (2004) 74–78, <http://dx.doi.org/10.1002/adem.200300507>.
- [11] M.-H. Chuang, M.-H. Tsai, W.-R. Wang, S.-J. Lin, J.-W. Yeh, Microstructure and wear behavior of AlxCo<sub>1.5</sub>CrFeNi<sub>1.5</sub>Ti<sub>y</sub> high-entropy alloys, *Acta Mater.* 59 (2011) 6308–6317, <http://dx.doi.org/10.1016/j.actamat.2011.06.041>.
- [12] J.-M. Wu, S.-J. Lin, J.-W. Yeh, S.-K. Chen, Y.-S. Huang, H.-C. Chen, Adhesive wear behavior of AlxCoCrCuFeNi high-entropy alloys as a function of aluminum content, *Wear* 261 (2006) 513–519, <http://dx.doi.org/10.1016/j.wear.2005.12.008>.
- [13] H. Hadraba, Z. Chlup, A. Dlouhy, F. Dobes, P. Roupova, M. Vilemova, J. Matejicek, Oxide dispersion strengthened CoCrFeNiMn high-entropy alloy, *Mater. Sci. Eng.: A* 689 (2017) 252–256, <http://dx.doi.org/10.1016/j.msea.2017.02.068>.
- [14] Z. Wu, H. Bei, F. Otto, G.M. Pharr, E.P. George, Recovery, recrystallization, grain growth and phase stability of a family of FCC-structured multi-component equiatomic solid solution alloys, *Intermetallics* 46 (2014) 131–140, <http://dx.doi.org/10.1016/j.intermet.2013.10.024>.
- [15] B. Gludovatz, A. Hohenwarter, K.V.S. Thurston, H. Bei, Z. Wu, E.P. George, R.O. Ritchie, Exceptional damage-tolerance of a medium-entropy alloy CoCrNi at

- cryogenic temperatures, *Nat. Commun.* 7 (2016) 10602, <http://dx.doi.org/10.1038/ncomms10602>.
- [16] Z. Wu, H. Bei, G.M. Pharr, E.P. George, Temperature dependence of the mechanical properties of equiatomic solid solution alloys with face-centered cubic crystal structures, *Acta Mater.* 81 (2014) 428–441, <http://dx.doi.org/10.1016/j.actamat.2014.08.026>.
- [17] S. Fang, W. Chen, Z. Fu, Microstructure and mechanical properties of twinned Al<sub>0.5</sub>CrFeNiCo<sub>0.3</sub>Co<sub>0.2</sub> high entropy alloy processed by mechanical alloying and spark plasma sintering, *Mater. Des.* 54 (2014) 973–979, <http://dx.doi.org/10.1016/j.matdes.2013.08.099>.
- [18] I. Moravcik, J. Cizek, P. Gavendova, S. Sheikh, S. Guo, I. Dlouhy, Effect of heat treatment on microstructure and mechanical properties of spark plasma sintered AlCoCrFeNiTi<sub>0.5</sub> high entropy alloy, *Mater. Lett.* 174 (2016) 53–56, <http://dx.doi.org/10.1016/j.matlet.2016.03.077>.
- [19] H. Tsukamoto, Microstructure and indentation properties of ZrO<sub>2</sub>/Ti functionally graded materials fabricated by spark plasma sintering, *Mater. Sci. Eng.: A* 640 (2015) 338–349, <http://dx.doi.org/10.1016/j.msea.2015.06.005>.
- [20] F. Lomello, G. Bonnefont, Y. Leconte, N. Herlin-Boime, G. Fantozzi, Processing of nano-SiC ceramics: densification by SPS and mechanical characterization, *J. Eur. Ceram. Soc.* 32 (2012) 633–641, <http://dx.doi.org/10.1016/j.jeurceramsoc.2011.10.006>.
- [21] I. Sulima, P. Putyra, P. Hyjek, T. Tokarski, Effect of SPS parameters on densification and properties of steel matrix composites, *Adv. Powder Technol.* 26 (2015) 1152–1161, <http://dx.doi.org/10.1016/j.apt.2015.05.010>.
- [22] ISO 6892 - 1, The tensile strength test was performed using 2 Metallic materials – tensile testing – Part 1: method of test at room temperature, 2009.
- [23] R. Leisure, F.A. Willis, Resonant ultrasound spectroscopy, *J. Phys.: Condens. Matter* 9 (1997) 6001, <http://dx.doi.org/10.1088/0953-8984/9/28/002>.
- [24] A. Migliori, J.D. Maynard, Implementation of a modern resonant ultrasound spectroscopy system for the measurement of the elastic moduli of small solid specimens, *Rev. Sci. Instrum.* 76 (2005) 7, <http://dx.doi.org/10.1063/1.2140494>.
- [25] A. Haglund, M. Koehler, D. Catoor, E.P. George, V. Keppens, Polycrystalline elastic moduli of a high-entropy alloy at cryogenic temperatures, *Intermetallics* 58 (2015) 62–64, <http://dx.doi.org/10.1016/j.intermet.2014.11.005>.
- [26] P. Sedláč, H. Seiner, J. Zídek, M. Janovská, M. Landa, Determination of all 21 independent elastic coefficients of generally anisotropic solids by resonant ultrasound spectroscopy: benchmark examples, *Exp. Mech.* 54 (2014) 1073–1085, <http://dx.doi.org/10.1007/s11340-014-9862-6>.
- [27] Z. Zhang, M.M. Mao, J. Wang, B. Gludovatz, Z. Zhang, S.X. Mao, E.P. George, Q. Yu, R.O. Ritchie, Nanoscale origins of the damage tolerance of the high-entropy alloy CrMnFeCoNi, *Nat. Commun.* (2015), <http://dx.doi.org/10.1038/ncomms10143>.
- [28] S. Curtze, V.T. Kuokkala, Dependence of tensile deformation behavior of TWIP steels on stacking fault energy, temperature and strain rate, *Acta Mater.* 58 (2010) 5129–5141, <http://dx.doi.org/10.1016/j.actamat.2010.05.049>.
- [29] G. Frommeyer, x.U. Br. uuml, P. Neumann, Supra-ductile and high-strength manganese-TRIP/TWIP steels for high energy absorption purposes, *ISIJ Int.* 43 (2003) 438–446, <http://dx.doi.org/10.2355/isijinternational.43.438>.
- [30] L. Chen, Y. Zhao, X. Qin, Some aspects of high manganese twinning-induced plasticity (TWIP) steel, a review, *Acta Metall. Sin. (Engl. Lett.)* 26 (2013) 1–15, <http://dx.doi.org/10.1007/s40195-012-0501-x>.
- [31] D.T. Pierce, J.A. Jiménez, J. Bentley, D. Raabe, J.E. Wittig, The influence of stacking fault energy on the microstructural and strain-hardening evolution of Fe–Mn–Al–Si steels during tensile deformation, *Acta Mater.* 100 (2015) 178–190, <http://dx.doi.org/10.1016/j.actamat.2015.08.030>.
- [32] M. Umemoto, K. Tsuchiya, Z.G. Liu, S. Sugimoto, Tensile stress-strain analysis of single-structure steels, *Metall. Mater. Trans. A* 31 (2000) 1785–1794, <http://dx.doi.org/10.1007/s11661-006-0249-x>.
- [33] S. Asgari, E. El-Danaf, S.R. Kalidindi, R.D. Doherty, Strain hardening regimes and microstructural evolution during large strain compression of low stacking fault energy fcc alloys that form deformation twins, *Metall. Mater. Trans. A* 28 (1997) 1781–1795, <http://dx.doi.org/10.1007/s11661-997-0109-3>.
- [34] I. Gutierrez-Urrutia, D. Raabe, Dislocation and twin substructure evolution during strain hardening of an Fe–22 wt% Mn–0.6 wt% C TWIP steel observed by electron channeling contrast imaging, *Acta Mater.* 59 (2011) 6449–6462, <http://dx.doi.org/10.1016/j.actamat.2011.07.009>.
- [35] A.L. Morales, A.J. Nieto, J.M. Chicharro, P. Pintado, Field-dependent elastic modulus and damping in pure iron, nickel and cobalt, *J. Magn. Magn. Mater.* 322 (2010) 1952–1961, <http://dx.doi.org/10.1016/j.jmmm.2010.01.013>.
- [36] J.A. Roberson, H.A. Lipsitt, Elastic behavior of polycrystalline chromium near the Néel temperature, *J. Appl. Phys.* 36 (1965) 2843–2848, <http://dx.doi.org/10.1063/1.1714591>.
- [37] H. Holleck, Material selection for hard coatings, *J. Vac. Sci. Technol. A: Vac. Surf. Films* 4 (2661) (1986) 1986, <http://dx.doi.org/10.1116/1.573700>.
- [38] A.F. Mirza, L.D. Chen, A unified model for the prediction of yield strength in particulate-reinforced metal matrix nanocomposites, *Materials* 810 (2015) 3390.
- [39] C. Herrera, D. Ponge, D. Raabe, Design of a novel Mn-based 1 GPa duplex stainless TRIP steel with 60% ductility by a reduction of austenite stability, *Acta Mater.* 59 (2011) 4653–4664, <http://dx.doi.org/10.1016/j.actamat.2011.04.011>.
- [40] H. Dong, Y.X. Gan, Y. Weng, SpringerLink, Advanced steels the recent scenario in steel science and technology. ISBN-10: 364217664X, 2011.
- [41] M.J. Yao, K.G. Pradeep, C.C. Tasan, D. Raabe, A novel, single phase, non-equiatomic FeMnNiCoCr high-entropy alloy with exceptional phase stability and tensile ductility, *Scr. Mater.* 72–73 (2014) 5–8, <http://dx.doi.org/10.1016/j.scriptamat.2013.09.030>.
- [42] Z. Wang, I. Baker, Interstitial strengthening of a f.c.c. FeNiMnAlCr high entropy alloy, *Alloy. Mater. Lett.* 180 (2016) 153–156, <http://dx.doi.org/10.1016/j.matlet.2016.05.122>.
- [43] I.S. Wani, T. Bhattacharjee, S. Sheikh, Y.P. Lu, S. Chatterjee, P.P. Bhattacharjee, S. Guo, N. Tsuji, Ultrafine-grained AlCoCrFeNi<sub>2.1</sub> eutectic high-entropy alloy, *Mater. Res. Lett.* (2016) 1–6, <http://dx.doi.org/10.1080/21663831.2016.1160451>.
- [44] B. Schuh, F. Mendez-Martin, B. Völker, E.P. George, H. Clemens, R. Pippan, A. Hohenwarter, Mechanical properties, microstructure and thermal stability of a nanocrystalline CoCrFeMnNi high-entropy alloy after severe plastic deformation, *Acta Mater.* 96 (2015) 258–268, <http://dx.doi.org/10.1016/j.actamat.2015.06.025>.
- [45] L. Liu, J.B. Zhu, C. Zhang, J.C. Li, Q. Jiang, Microstructure and the properties of FeCoCuNiSn<sub>x</sub> high entropy alloys, *Mater. Sci. Eng.: A* 548 (2012) 64–68, <http://dx.doi.org/10.1016/j.msea.2012.03.080>.